Real-Time and Near Real-Time Displacement Monitoring With GNSS Observations in the Mining Activity Areas

Damian Tondaś, Kamil Kazmierski, and Jan Kapłon

***Abstract*—Ground deformations can be determined via various measurement methods, such as levelling, laser scanning, satellite navigation systems, synthetic aperture radar, and many others. In this article, the authors present cross-validation displacement monitoring results obtained via real-time (RT) and near real-time (NRT) global navigation satellite system calculation scenarios. To verify and validate the quality of RT and NRT long-term displacements, an independent postprocessing (P-P) service was established. The study area was located in the Upper Silesian coal mining region in Poland. The verification procedure for the RT and NRT systems included a demonstration of the achieved accuracy, the time span required to detect a significant displacement, and the determination of the minimum detectable value of deformation. Regarding the P-P data source, the NRT service had root mean square (RMS) errors of approximately 2 and 4 mm for the horizontal components, while the RT errors ranged from 5 to 10 mm. In the vertical direction, the NRT strategy had RMS errors of 5–6 mm, while the RT service achieved the accuracy of 10 mm. The minimum detectable values of deformation for the NRT procedure were 5, 7, and 11 mm in the northern, eastern, and up directions, respectively. For the RT system, the significant values were determined to be 10 and 15 mm for the horizontal and 20 mm for the vertical components.**

***Index Terms*—Global navigation satellite system (GNSS) displacement monitoring, mining deformations, near real-time (NRT), real-time (RT).**

I. Introduction

MONITORING deformations caused by underground mining activity using global navigation satellite system (GNSS) measurements has been a global standard for two decades (e.g., [1], [2], [3], [4], [5]). These monitoring techniques combine epoch measurements with one of the following methods: the rapid-static method with double difference (DD) phase observations [1], the static precise point positioning (PPP) method [6], the real-time kinematic (RTK) method [2], and PPP [3], and a postprocessing (P-P) method [7]. The P-P monitoring mode is mostly done in DD as in the daily processing performed for the International GNSS Service (IGS) or the EUREF Permanent Network (EPN).

The particular GNSS observation technique determines subsequent parameters that have a direct impact on the feasibility and precision of long-term ground deformation monitoring. Among the mentioned criteria, we can distinguish the character of conducted measurements (permanent or campaign), the type of GNSS products (real-time, ultrarapid, rapid, final), the interval of observations (e.g., 20 Hz, 10 Hz, 1 s, 30 s), or the quality of the GNSS equipment (geodetic, low-cost) [8].

The GPS-RTK campaign approach for mining deformation monitoring was presented by Gao et al. [9]. The authors performed surveys with 1 s and 20 Hz intervals of observations and established the accuracy on level 10 mm in vertical and 20–40 mm in horizontal directions. However, the described method was not concerned with the determination of potential ground displacement—the survey was taken only once on October 31, 2010. The rapid-static campaign method above the extracted mining panels was introduced by Doležalová et al. [1]. The calculation of GPS observations was carried out in DD mode, however, the type of applied GNSS products and the interval of collected data were not specified. The authors considered only vertical subsidence, achieving a surveying accuracy of 5 to 20 mm for the spatial position of a point (XYZ). Within the study, information about the error estimation procedure also was not defined. The permanent static measurements across long-wall mining areas were performed by Lian et al. [10]. To estimate the daily three-dimensional (3-D) positions, based on GPS, GLONASS, and BeiDou observations, the DD technique was applied. After 90 days of investigation, the greatest horizontal displacement was established around 1.8 m, while the maximum vertical subsidence was equal to –3.0 m. During the research, the authors did not manage to calculate the real uncertainties of the given results, providing only the precision of used GNSS devices as 3 and 5 mm in the horizontal and vertical directions, respectively.

The GNSS technology is a common method used to monitor ground displacements, however, investigation of the feasibility and accuracy of particular GNSS techniques is not commonly tested. Xu et al. [6] verified the ability of PPP service to detect

Manuscript received 18 October 2022; revised 21 April 2023; accepted 18 June 2023. Date of publication 29 June 2023; date of current version 10 July 2023. This work was supported by the Wrocław Centre of Networking and Supercomputing (www.wcss.wroc.pl): computational grant using MATLAB Software License No: 101979 and in part by the APC/BPC is co-financed by Wrocław University of Environmental and Life Sciences. This study was conducted according to EPOS – European Plate Observing System and EPOS-PL+ cofinanced by the European Union from the funds of the European Regional Development Fund POIR.04.02.00-14-A003/16 and POIR.04.02.00-00-C005/19. *(Corresponding author: Damian Tondaś.)*

The authors are with the Institute of Geodesy and Geoinformatics, Wrocław University of Environmental and Life Sciences, 50-357 Wrocław, Poland (e-mail: damian.tondas@upwr.edu.pl; kamil.kazmierski@upwr.edu.pl; jan.kaplon@upwr.edu.pl).

Digital Object Identifier 10.1109/JSTARS.2023.3290673

mining deformation using various quality metrics. As a test site, the IGS geodetic BJFS station was selected. The case study was performed based on GPS data collected from March 7, 2008, 2009, and 2010. The interval of observations was equal to 30 s and the time series of coordinates was established in P-P mode using the IGS final products. The reference dataset was created using Scripps Orbit and Permanent Array Centre. The vertical and horizontal root mean square (RMS) errors of the PPP method were estimated as "below 2 cm" and the minimum detectable 3-D ground deformation was described there as 5–25 mm.

The main aim of the presented paper is to systematize existing knowledge on the reliability and accuracy of GNSS estimation services regarding permanent long-term ground displacement monitoring. As a part of the EPOS-PL project's (https://epos-pl.eu/) GNSS Data Research Infrastructure Centre (Polish abbreviation CIBDG) [11], Wrocław University of Environmental and Life Sciences established a local network of GNSS stations and a computing GNSS center to monitor ground deformations in the Upper Silesia coal mining area. The CIBDG computing center processes data in real-time using the PPP-RT method [12], [13] and the near real-time DD calculation scenario [14]. The CIBDG is one of the research infrastructure centers involved in investigating the mechanisms of anthropogenic threats related to underground mining for the EPOS-PL project [11]. The data and results collected within the project are made available on the IS-EPOS platform [15] through the Thematic Core Service Anthropogenic Hazards (https://tcs.ah-epos.eu/) using the so-called multidisciplinary upper Silesian episodes (MUSE).

This research presents the results of two years of monitoring ground deformations in coal mining areas in Upper Silesia in Poland. The long-term subsidence events were verified via real-time (RT) and near real-time (NRT) GNSS techniques and cross-referenced with a daily P-P solution. During analysis, several factors were taken into account to characterize the feasibility and accuracy of displacement determinations, e.g., the minimum significant value concerning deformation detection, and the minimum time span of its occurrence. Section II provides a detailed description of the GNSS processing strategies. In Section III, the methodology used for the verification and detection of deformations is described. Section IV demonstrates the results concerning displacement monitoring capabilities. In Section V, we summarize and discuss all the results obtained.

II. Data Processing Strategies

The RT and NRT GNSS displacement monitoring methods present various significant differences in computational strategies. Among these discrepancies, the most fundamental referred to the technique of position determination and the interval of calculations. The RT service is based on the absolute PPP method running in 30-s intervals, while the NRT processing scenario relies on a relative DD solution with a 15-min sampling rate of estimation. Therefore, to ensure the integrity of the reference data for the RT and NRT systems in the Upper Silesian area, it was necessary to establish an independent GNSS calculation strategy. Separate computations were carried out in P-P mode based on the final GNSS products.

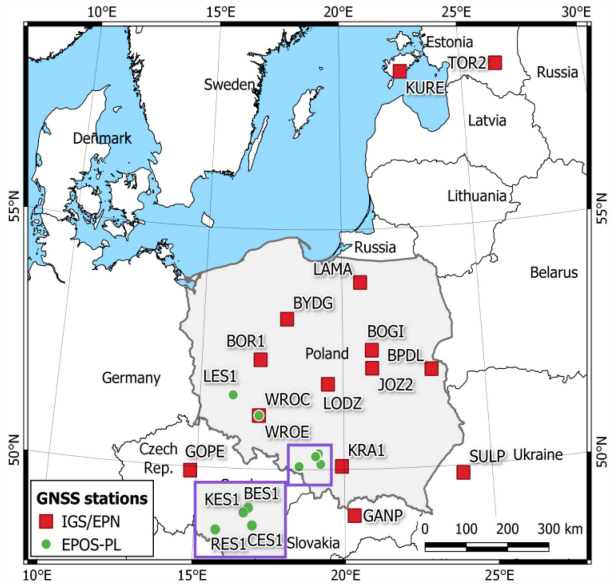

Fig. 1. Locations of GNSS stations involved in the DD network for the P-P and NRT systems (red rectangles and green dots, respectively) and used in PPP by the PPP-RT service (green dots).

Furthermore, in this study, another GNSS method for long-term displacement monitoring was tested (but not in RT or NRT mode). This service is based on Bernese GNSS Software v. 5.2 [16] and normal equations (NQ0) stored during the NRT computations, which are combined in the so-called stacked-NRT solution (NRT-S). The stacking procedure was essential to determine the actual coordinates of all processing stations, providing a priori information for the NRT calculations. As a result, a time series with a daily data interval was obtained for the deformations. A detailed description of the differences in the presented calculation strategies is shown in Table I.

A. Postprocessing (P-P) Service

The multi-GNSS P-P solution was performed using the DD technique. In this approach, 14 stations involved in the IGS and EPN networks served as reference points. To obtain the coordinates and velocities of the reference stations in the ITRF2014 frame, we applied data from a SINEX format file (EPN_A_IGS14.SNX). The SINEX file, created by CATREF software [24], was acquired from the EPN FTP server (ftp://epncb.oma.be/). The set of reference stations was the same for the P-P, NRT, and NRT-S solutions (see Fig. 1).

The P-P solution relied on GPS, GLONASS, and Galileo observations and was performed in the Bernese GNSS Software v. 5.2 [16] with a daily computational interval. Furthermore, the processing scenario was based on the final precise GNSS products (see Table I). These products included the orbits and clocks of the multi-GNSS satellites obtained through the Center for Orbit Determination in Europe (CODE, [22]). To ensure the highest precision in the calculations, individual antenna calibration models were used for the EPN stations. The antenna calibration data were acquired from the epnbc_14.atx file (ftp://epncb.oma.be/).

TABLE I
SUMMARY OF THE PPP-RT, NRT, NRT-S, AND P-P STRATEGIES

Parameter	GNSS service			
	real-time (PPP-RT)	near real-time (NRT)	stacked NRT (NRT-S)	post-processing (P-P)
Technique	PPP	DD	DD	DD
Interval of calculations	30 s	15 min	1 day	1 day
Latency of results	<1 s	5–14 min	2 h	2 weeks
Time window	–	6 h	2 weeks	1 day
Observables	pseudo-range and carrier phase	pseudo-range and carrier phase	NQ0 files from NRT	pseudo-range and carrier phase
Frequencies (RINEX 3.05 notation)	GPS: L1/L2, Galileo: E1/E5a	GPS: L1/L2, GLONASS: G1/G2	–	GPS: L1/L2, GLONASS: G1/G2, Galileo: E1/E5a
Inter-system weighting	elevation (e) dependent: $\sin(e)$	zenith (z) dependent: $\cos(z)^2$	–	zenith (z) dependent: $\cos(z)^2$
Cut-off angle	3°	5°	–	5°
Troposphere delay MF and a priori data	UNB3m mapping functions [17]	dry VMF1-FC [18]	–	dry VMF1 [19]
Site-specific ZTD correction with MF coefficients	wet delay estimated as a $5mm/\sqrt{h}$ random walk process	wet VMF1-FC [18] with a $1mm/\sqrt{h}$ relative constraint	–	wet VMF1 [19] with a $1m/\sqrt{h}$ relative constraint
ZTD horizontal gradient	linear horizontal estimation [20]	linear horizontal estimation [20] with a $0.1mm/\sqrt{h}$ relative constraint	–	linear horizontal estimation [20] with a $0.1m/\sqrt{h}$ relative constraint
Satellite orbits and clocks	fixed from real-time CNES stream (SSRA00CNE0)	IGS ultrarapid [21]	–	CODE final [22]
Receiver clock	estimated GPS clock and ISB for other systems	–	–	–
Code and phase biases	absolute, from real-time CNES stream (SSRA00CNE0)	–	–	–
Ambiguity resolution	–	L6/L3, L5/L3, QIF	–	L6/L3, L5/L3, QIF
Solution type	undifferentiated and not combined with float ambiguities	minimum constraint on translation	minimum constraint on translation	minimum constraint on translation
Correction models	phase wind-up, relativistic delays, solid earth tides, receiver antenna phase center offset, and variation [23]	IGS Earth rotation parameters, post-seismic deformations, ionosphere-free combination in final solution, ocean and atmospheric tidal loading, antenna phase center offset, and variation	post-seismic deformations, ionosphere-free combination in final solution	CODE earth rotation parameters, post-seismic deformations, ionosphere-free combination in the final solution, ocean and atmospheric tidal loading, CODE's Global Ionosphere Maps for QIF strategy, antenna phase center offset, and variation

The method to resolve phase ambiguities in the assigned network vectors was determined according to their approximate lengths. For the longest baselines of more than 200 km, a strategy based on the Melbourne–Wübbena linear combination (L6) was adopted. In the subsequent run, the ionosphere-free (L3) linear combination was processed, the Melbourne–Wübbena ambiguities were introduced as known, and the narrow-lane (L1) ambiguities were resolved. For medium-length vectors (between 20 and 200 km), the wide-lane linear combination (L5) was used to initial estimate integer phase ambiguities to be introduced in the

following narrow-lane ionosphere-free (L3) phase ambiguities estimation. The quasi-ionosphere-free (QIF) strategy was also applied to the remaining real-valued ambiguities. For baselines shorter than 20 km, the L1&L2 frequencies were used independently for ambiguity resolution [16]. To verify and validate the quality of the P-P results, we compared the P-P coordinate time series with an external and independent data source- the EUREF combined coordinate solution (Section II-E).

B. Near Real-Time (NRT) Methods

The NRT service, also called the ultrafast NRT, was implemented within the EPOS-PL project. The most important characteristic of the ultrafast NRT service is a shortening of the usual hourly interval between the NRT GNSS data processing to a 15-min interval with 5–14 min of latency from the last observation to the processing results. The ultrafast method of DD estimation was developed based on an in-house algorithm [14]. In the first minute of each quadrant, the ultrafast NRT system acquires GNSS observations and products simultaneously. Therefore, the remaining time (14 min) is used for the calculations of Bernese GNSS Software v 5.2 [16]. The data required for the calculations in this article were gathered via RTCM streams (www.igs-ip.net, www.euref-ip.net, ltg10.gislab.up.wroc.pl) and FTP services (ftp.aiub.unibe.ch/, ftp://igs.ensg.ign.fr/, nonpublic ASG-EUPOS FTP server).

The NRT and P-P strategies were implemented using similar parameters and methods (see Table I). Among the crucial ones, we can distinguish the intersystem observation weighting, the elevation of the cut-off angle, and the minimum constraint on translation solution type. Despite several similarities, the differences involved such parameters as: calculation intervals (15 min versus 1 day), estimation time windows (6 hours versus 1 day), GNSS observations (GR versus GRE), GNSS product types (IGS ultrarapid versus CODE final), and tropospheric mapping functions (VMF1-FC versus VMF1) with different relative constraints on ZTD and linear gradient variations.

In order to compare the results of the NRT systems in the time resolution domain of the P-P service, an average daily solution was also calculated. The NRT dataset obtained with a daily time span was defined as NRT-D. Note that there is a very strong connection between the NRT and the NRT-D results.

C. Stacked NRT Solution (NRT-S)

The main purpose of the stacked NRT solution was to ensure the initial coordinates and velocities for all GNSS stations included within the NRT processing without necessarily introducing any new GNSS observations. In contrast to the NRT-D approach, where the averaged data for a particular day were considered, the results of the NRT-S solution were determined with a combination of the normal equations stored within the previous two weeks. The evaluation procedure was launched in a daily mode two hours after the end of the previous day. The calculation strategy was based on No-Net-Translation and the minimum constraint solution. The Helmert translation control for fiducial stations, with thresholds of 15 mm for the horizontal components and 30 mm in the vertical direction, was also applied. The coordinates were established at midday on the previous day. The summary of the NRT-S strategy is presented in Table I.

D. PPP Real-Time (RT) Variants

GNSS observations were also processed in an absolute manner with the PPP technique. Continuous estimation in a real-time regime was performed with corrections prepared by the Centre National d'Études Spatiales (CNES) via the Internet RTCM stream at the mount point SSRA00CNE0. The observations were processed with the in-house developed software GNSS-WARP (Wroclaw Algorithm for Real-Time Positioning, [12]). The calculation strategy is described in detail in Table I. The observations were processed continuously without reinitialization (PPP-RT) at 30-s intervals. Additionally, the same set of data was calculated for each day separately. The last position in a day was considered in the further analyses (PPP-RT-D). Both processing methods were conducted using the strategy described in Table I.

E. Reference Solution (EUREF)

In this article, we used the EUREF combined coordinate solution as the reference data source for the multi-GNSS P-P service. The comparison allowed an assessment of the quality of station coordinates in the P-P mode. The overall evaluation was conducted using 14 reference stations belonging to the IGS and EPN networks. Details of the comparison are described in Section IV-A.

The EUREF results were created based on the daily GNSS solutions generated by the EPN analysis centers (ACs). The ACs process the observations of the assigned subnetwork according to the guidelines covering the analysis procedure and submission of the results (www.epncb.oma.be). As of 31/01/2022, there were 16 EPN ACs. To obtain the combined daily and weekly positions of the IGS and EPN stations, the ACs' normal equations were combined by the EPN AC Coordinator (ACC, http://www.epnacc.wat.edu.pl/) using Bernese GNSS software [16]. In the main calculation procedure, the daily outcomes were stacked together with the previous 10 weekly solutions and compared with the resulting combination using a 7-parameter transformation. Stations with coordinate residuals exceeding 15 mm for the horizontal components or 25 mm in the vertical direction were eliminated from the analyses.

The combined coordinate solutions were realized using No-Net-Translation and minimum constraint conditions in alignment with the IGS14 reference frame. The minimum constraints were imposed on IGS stations with coordinate differences that did not exceed thresholds of 8 mm in the horizontal direction and 15 mm for the vertical component. The combined daily and weekly coordinate solutions are available on the EPN server (ftp://epncb.oma.be/) in SINEX format (EUR*WWWWD*.SNX, where *WWWW* indicates GPS week and *D* indicates GPS day).

III. Verification of Deformation Detection Methods

During the study, it was necessary to adopt a universal methodology for comparing results within the temporal and spatial

domains. In the temporal domain, different intervals were used to achieve coordinate time series (30 s for PPP-RT, 15 min for NRT, and 1 day for PPP-RT-D, NRT-D, NRT-S, and P-P). Therefore, two separate manners of temporal cross-comparison were established. The first time domain was defined as a 15-min interval and was applied for PPP-RT, NRT, and P-P services (the PPP-RT data set was reduced, and the P-P results were linearly interpolated), while the second manner corresponded to a daily sampling and was used for PPP-RT-D, NRT-D, NRT-S, and P-P strategies.

In the case of the spatial domain, all described computational services used the geocentric ITRF2014 reference frame [25]. To avoid the impact of Euro-Asian plate drift, the coordinates were transformed to the ETRF2014 reference frame [26]. Afterward, for a better understanding of the local displacements occurrence, the geocentric coordinates were converted to the topocentric NEU frame indicated as follows:

$$\begin{bmatrix} N \\ E \\ U \end{bmatrix} = \begin{bmatrix} -\sin(B)\cos(L) & -\sin(B)\sin(L) & \cos(B) \\ -\sin(L) & \cos(L) & 0 \\ \cos(B)\cos(L) & \cos(B)\sin(L) & \sin(B) \end{bmatrix} \times \begin{bmatrix} X_i - X_{\text{ref}} \\ Y_i - Y_{\text{ref}} \\ Z_i - Z_{\text{ref}} \end{bmatrix} \tag{1}$$

where N, E, and U are the North, East, and Up topocentric coordinates, respectively; B and L are the longitude and latitude of the reference point, respectively; X_i, Y_i, and Z_i are the geocentric coordinates of the GNSS station determined for the ith computational epoch; and X_{ref}, Y_{ref}, and Z_{ref} are the geocentric coordinates of the reference epoch. The most illustrative way to present the variation in the position of a GNSS station over time is to use the first epoch as the reference value. Instead, to avoid adopting an outlier as the initial position, the averaged coordinates from the first five computational epochs were used as the reference values.

The cross-validation of the results obtained from a particular GNSS processing scenario was performed via statistical calculations. In relation to the reference database of coordinates, the following statistical parameters were determined: the residual values between two data sources estimated for the same ith epoch- res_i (2), the systematic error- BIAS (3), the standard deviation of the residuals- STD (4), and the root mean square error of the residuals- RMS (5)

$$\text{res}_i = x_i^v - x_i^r \tag{2}$$

$$\text{BIAS} = \frac{1}{n}\sum_{i=1}^{n} \text{res}_i \tag{3}$$

$$\text{STD} = \sqrt{\frac{1}{n}\sum_{i=1}^{n} (\text{res}_i - \text{BIAS})^2} \tag{4}$$

$$\text{RMS} = \sqrt{\text{BIAS}^2 + \text{STD}^2} \tag{5}$$

where x_i^v and x_i^r are the verified and reference values at the ith epoch, respectively, and n is the number of common epochs. The statistical analysis performed for the results achieved by the computational services gives a general quality overview of the obtained coordinates. However, a more detailed investigation of the significant occurrence of ground deformation with the minimum time span required to register it is described in the second part of the paper which uses the following:

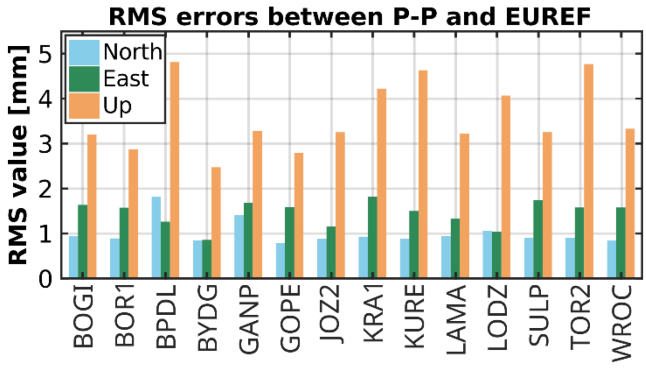

Fig. 2. RMS errors of the P-P solution in comparison to the EUREF final data source.

$$d_{\text{sig}} \geq \sqrt{\chi^2(k)} \cdot m_d \tag{6}$$

where d_{sig} is the significant deformation value, $\chi^2(k)$ represents the critical value of the chi-square distribution with k degrees of freedom for a one-sided test, and m_d is the RMS error of the deformation value. For a 0.05 level of significance and a single direction of displacement ($k = 1$), the χ^2 critical value is equal to 3.84.

IV. Comparative Analysis of Displacements

The analysis of RT and NRT displacement monitoring was performed in three sequential stages:

1) An investigation into whether the P-P computation could represent a source of reference data in further analyses (Section IV-A).
2) The cross-validation of the results obtained from particular GNSS service calculations via statistical computations (Section IV-B).
3) An investigation into the possibility of long-term deformation detection by the various computational GNSS systems (Section IV-C).

A. Verification of Postprocessing Service

In order to compare the P-P and EUREF solutions, time series of daily positions were analyzed for 14 common IGS and EPN stations. The investigation concerned the RMS errors for three topocentric components: North, East, and Up (see Fig. 2). To convert geocentric positions to topocentric frame, reference coordinates were required. Therefore, for each station, the initial positions were set as the average of the geocentric coordinates of the first five epochs of the EUREF dataset.

Based on the RMS error bar chart (see Fig. 2), it can be concluded that the quality of the determination of the horizontal components is very high. The RMS error value does not exceed 2 mm for any station. Moreover, for only two sites, the RMS

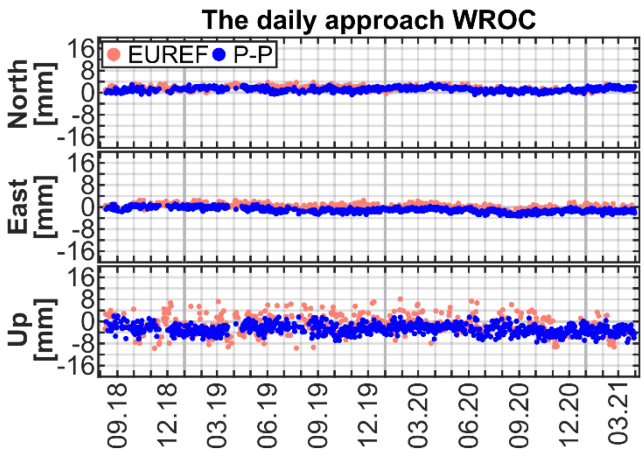

Fig. 3. Comparison of the P-P (blue dots) and the EUREF (orange dots) solutions for the topocentric time series of coordinates performed using the WROC IGS station.

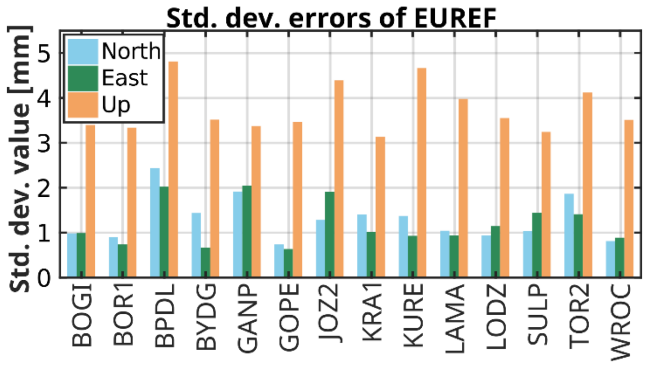

Fig. 4. Standard deviation of the EUREF solution for the topocentric time series of coordinates.

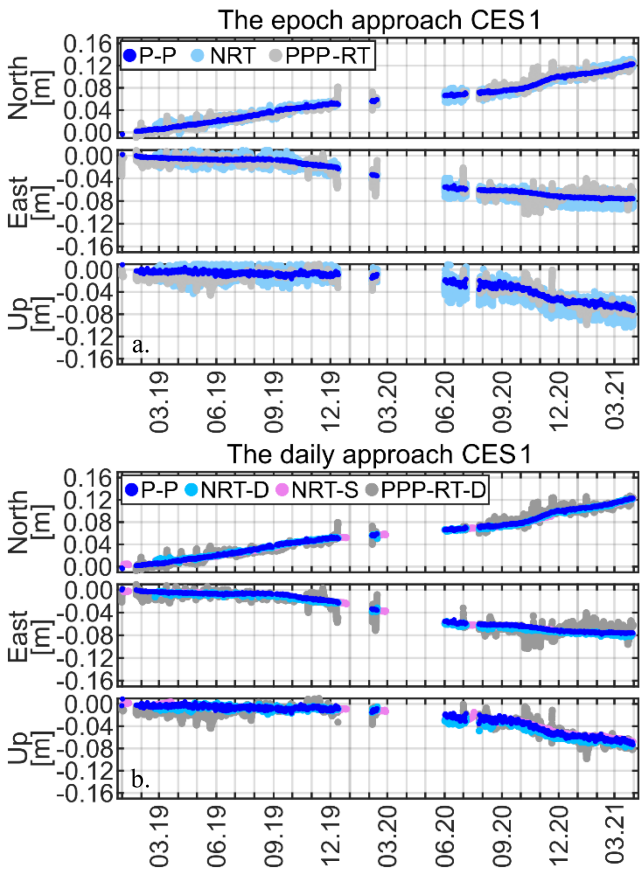

Fig. 5. Time series of coordinates for the CES1 EPOS-PL station in the ETRF2014 reference frame in the North, East, and Up directions, performed in the epoch (a) and daily (b) time frames.

values are greater than 1 mm for the North component (BPDL and GANP). The East RMS errors are slightly higher and are in the range of 1–2 mm.

On the contrary, the errors for the vertical component are almost two times larger in comparison to the horizontal directions. The RMS errors exceed 3 mm overall, furthermore, for four stations, the errors overrun 4 mm (BPDL, KRA1, KURE, and TOR2). Therefore, it was necessary to analyze the reason for the larger RMS errors in the vertical direction.

For this investigation, the P-P and EUREF datasets obtained for one of the stations (WROC) were compared. In Fig. 3, a slight BIAS (3) for the eastern component (–2 mm) can be observed in both solutions. Assuming a similar distribution of BIAS for the other stations, it can be concluded that this discrepancy affects RMS East values on the order of 1–2 mm. However, the most substantial variations in the time series occur in the vertical component. The larger noise can be observed for the EUREF dataset compared to the P-P system. To determine the noise rate, the *STD* (4) was calculated. A detailed analysis of the noise level in the EUREF time series for all stations is presented in Fig. 4.

The *STD* values of the EUREF solution demonstrate a similar distribution to the RMS errors between the EUREF and P-P data sources (see Figs. 2 and 4). Therefore, the larger RMS errors for the vertical component can be related to the internal noise level of the EUREF dataset. As a result of its verification, the P-P service can be used as a reference for the PPP-RT, PPP-RT-D, NRT, NRT-D, and NRT-S strategies.

B. *Verification of Real-Time and Near Real-Time Systems*

The main goal of the research was to investigate the possibility of monitoring ground deformations using RT or NRT GNSS procedures. The systems differ mainly in the manner of coordinates estimation, which essentially contributes to the accuracy of the obtained results. Therefore, the quality of the coordinate time series was verified through RMS errors in reference to the P-P database.

The area of interest for ongoing ground deformation monitoring was the Upper Silesia region. In this active mining territory of Poland, significant movements reaching up to 1.6 m/year, can be potentially observed using the interferometric synthetic aperture radar (InSAR) technique [27]. Hence, as part of the EPOS-PL project, four GNSS receivers were located in the expected subsidence areas. In this study, observations of two years' time span were analyzed. However, ground deformations were registered for only two stations: CES1, located in Chełm Śląski (see Fig. 5), and RES1, located in Rybnik (see Fig. 6). As mentioned in

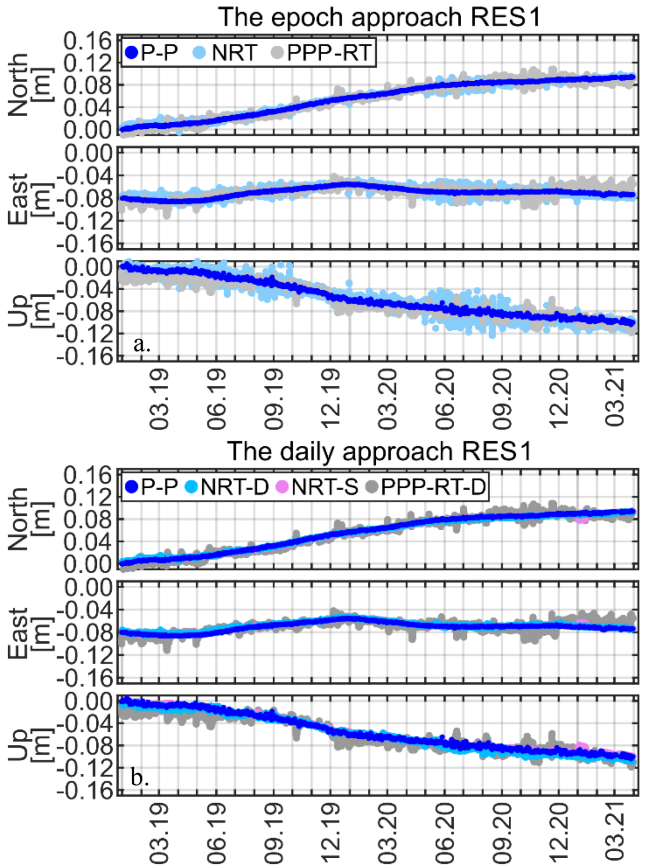

Fig. 6. Time series of coordinates for the RES1 EPOS-PL station in the ETRF2014 reference frame in the North, East, and Up directions, performed in the epoch (a) and daily (b) time frames.

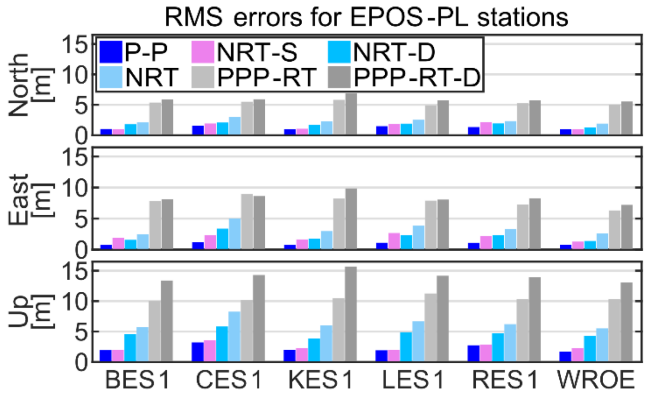

Fig. 7. Quality of the NRT-S, NRT-D, NRT, PPP-RT, and PPP-RT-D solutions in comparison to the P-P data source.

Section III, the verification of the RT and NRT systems was performed under two manners: (a) 15 min, and (b) daily.

The maximum deformation values for the CES1 station occurred at the end of the observation period and reached around 120 mm for the North and –80 mm for both East and Up directions. The northern displacement increased almost steadily from the beginning of the calculations, while the eastern and vertical components oscillated marginally and after several months the rate of movement increased. Around September 2019 the eastern displacements started growing rapidly, while the vertical component began to reach significantly higher values around the second half of 2020. Due to the lack of data for the CES1 station, caused by technical issues, it was not possible to observe the exact moment when vertical subsidence began.

During the two years of observations, the maximum displacements for the RES1 station reached around 90 mm for the North, 30 mm for the East, and –100 mm for the Up directions. The northern and vertical ground motions increased almost steadily, however, the movement observed in the eastern direction achieved relatively low values that varied over time. In the first stage of this displacement, slightly negative values were recorded (westward movements), and then the deformation reversed direction, reaching a peak around the end of 2019. In the last phase, the eastern displacement slowly began assuming the initial position.

Using the epoch-based approach [see Figs. 5(a) and 6(a)], it was challenging to recognize which system (NRT or PPP-RT) was more efficient in terms of monitoring deformations. For both methods, the noise of the output was higher than for the reference data source (P-P). However, the NRT results were much more consistently distributed. The PPP-RT data showed more long-term tendencies for both stations than the reference P-P solution, e.g., the RT service obtained lower values for Up from 01/2019 to 08/2019 and greater values for East from 12/2020 to the end of 03/2021. Furthermore, some significant coordinate variations of the PPP-RT process were also noticeable, especially for the CES1 station [see Fig. 6(a)].

In the daily interval domain [see Figs. 5(b) and 6(b)], a high agreement can be observed between the NRT-D and NRT-S results with reference to the P-P service. However, the displacements registered by the PPP-RT-D processing were characterized by a much higher level of measurement noise. All the discrepancies and similarities mentioned above directly contributed to the RMS errors. Fig. 7 shows the summarized accuracies for all the analyzed EPOS-PL stations. The uncertainty values were defined as the amounts of measurement noise from particular computational methods. Thus, a polynomial trend was estimated and eliminated separately for the North, East, and Up time series according to the P-P service results. Furthermore, after trend removal, the low-frequency residual values were filtered to obtain a normal distribution for the measurement noise.

The P-P service obtained the lowest RMS values, however, the established errors were not affected by the BIAS values-based on P-P data the polynomial function was estimated. Nevertheless, the NRT-S and NRT-D services presented similar or slightly larger horizontal error values within the range of 1–2 mm. The exceptions consisted of eastward values for stations LES1 and CES1, where the errors reached around 3 mm for both the NRT-S and NRT-D services. In horizontal domains, the NRT system achieved RMS errors in the range of 2–4 mm, with the exception of the eastern direction for the CES1 station (5 mm). In contrast, the PPP-RT and PPP-RT-D scenarios had errors over 5 mm, which were highest at stations CES1 (9 mm) and KES1 (10 mm) in the eastern direction.

In terms of vertical components, both the P-P and NRT-S services achieved similar errors, which were within 2–3 mm for

TABLE II
NUMBER OF DAYS AFTER THE SIGNIFICANT DEFORMATION VALUE IN A SPECIFIED DIRECTION COULD BE OBSERVED VIA GNSS SERVICE

Station	Direction	GNSS service [days]					
		P-P	NRT-S	NRT-D	NRT	PPP-RT	PPP-RT-D
CES1	N	34	37	43	52	86	99
	E	32	63	70	142	303	310
	U	101	144	316	401*	537	592
RES1	N	17	23	24	33	103	123
	E	15	47	49	94	268	277
	U	44	65	108	123	180	222

Note: *Due to a lack of observations, it was not possible to determine the exact moment when the significant value occurred

TABLE III
MINIMUM DEFORMATION THAT CAN BE DETECTED BY THE INDICATED GNSS SERVICE

Component	GNSS service [mm]					
	P-P	NRT-S	NRT-D	NRT	PPP-RT	PPP-RT-D
N	3	3	4	5	10	12
E	2	4	4	7	15	16
U	4	5	9	11	20	28

all stations. The NRT-D errors exceeded 4 mm, recording the highest RMS error for the CES1 station (6 mm). For the NRT system, the accuracy range was 5-6 mm, excluding station CES1 (8 mm). The PPP-RT solution achieved or slightly exceeded 10 mm RMS errors, while the least successful adjustment to the vertical reference data occurred for the PPP-RT-D. For this procedure, the average RMS errors were between 13 and 14 mm with a maximum of 16 mm for the KES1 station.

C. Detection of Deformations

The possibility of long-term ground deformation monitoring via GNSS services was analyzed using two procedures. In the first approach, the minimum time spans required to detect deformations at the CES1 and RES1 stations were investigated (see Table II). The second approach involved determining the minimum displacement value that could be detected by each GNSS strategy (see Table III). The determination of these two parameters was mainly related to the accuracy of the estimation of the particular GNSS service and was performed using inequality (6).

1) Time Span Approach: In the time span approach, the verification was carried out to identify the number of days since a significant value in a specified direction could be observed via the particular GNSS scenario. The initial epoch for all GNSS systems was 01/01/2019, therefore, the number of days in Table II always refers to the days from that date. The parameter was determined based on the displacement values and uncertainties estimated for stations CES1 and RES1. The analysis was carried out for the P-P, NRT, and RT services. It should be noted that the number of days depended on the movement rates of the North, East, and Up components.

As mentioned in Section IV-B, for station CES1, the northward displacement increased constantly from the beginning of the calculation. For the P-P and NRT-S systems, significant values in the northern direction were observed after around a month (34 and 37 days, respectively). For the other GNSS services, this time ranged from around 1.5 months for the NRT-D and NRT (43 and 52 days) to around 3 months for the RT systems (86 and 99 days).

The eastern component rate of the CES1 station started to increase after approximately nine months, however, for the P-P strategy, a significant value could be defined after around one month (32 days). The NRT service group recorded significant displacements after 2 months (NRT-S and NRT-D) and after 4 months (NRT). Overall, the real-time calculations were able to register significant values at the end of 2019 when eastern deformation began increasing (10th month).

In the first year of observation, the vertical subsidence of the CES1 station were not as dynamic as the horizontal displacements. Using the P-P scenario, a significant deformation was observed after 3.5 months (101 days), while the NRT-S system took 4 months (144 days). For the NRT-D and NRT, this time ranged from 10 to 13 months (316 and 401 days, respectively), whereas for PPP-RT and PPP-RT-D, it took from 18 to 20 months (537 and 592 days, respectively). However, for the NRT system, it was not possible to determine the exact moment when the significant value occurred due to a lack of observations (it could have taken less time).

In the case of the RES1 station, the northern movement continuously increased with time. For the P-P strategy, a significant value for the North component was observed in the middle of the first month (17 days). For the NRT-S and NRT-D, this time span was less than a month (23 and 24 days, respectively), whereas the NRT system took just slightly more than one month (33 days), the PPP-RT service registered displacement after around 3.5 months (103 days), while the PPP-RT-D procedure took over 4 months (123 days).

The eastern component of RES1 achieved its maximum value of approximately 30 mm around the end of 2019, and after several months, the deformation regressed to the initial position. The P-P system was able to detect ground motion that occurred in the western direction in the middle of the first month (15 days), while the NRT-S and NRT-D could detect this movement after 1.5 months (47 and 49 days, respectively). For the NRT computations, a significant value for the eastern direction was observed after around 3 months (94 days), and RT services picked up movement in the third quarter of the year (268 and 277 days for PPP-RT and PPP-RT-D, respectively).

The vertical subsidence increased almost continuously over time. A considerable value was observed after around 1.5 months (44 days) for the P-P scenario, after around 2 months (65 days) for the NRT-S, after 3.5 months (108 days) for the NRT-D, and after around 4 months (123 days) for the NRT. The RT systems were able to detect a subsequent displacement after 6 and 7.5 months (for the PPP-RT and PPP-RP-D, respectively).

2) Minimum Detectable Value of Displacement: In the second approach, the minimum detectable value of the deformation was investigated (see Table III). The evaluation was performed using the residuals from all EPOS-PL stations. The values were determined as a measurement noise obtained from coordinate datasets without the polynomial trend, which was estimated according to the results of the P-P approach. Furthermore, after removing the trend, the low-frequency residual values were filtered out to obtain a normal distribution for the measurement noise. The most successful results were achieved for the P-P service (3 and 2 mm for the horizontal and 4 mm for the vertical components). For the GNSS NRT calculation methods, the minimum detectable values of horizontal deformation did not exceed 10 mm. In this domain, the northern displacements were within 3 mm (NRT-S) to 5 mm (NRT), while for the eastern direction, the values were 4 mm for both NRT-S and NRT-D, and 7 mm for the NRT procedure.

In the case of the vertical component for the NRT methods, only the NRT system slightly exceeded a value of 10 mm.

For the RT services, significant values were determined to be 10 and 15 mm for the horizontal and 20 mm for the vertical components. The most unsatisfactory results were obtained for the PPP-RT-D (12 mm for N, 16 mm for E, and 28 mm for U). In addition to having the lowest detectability, the PPP-RT-D computations were performed in a daily interval mode.

V. Conclusion

In contrast to the point-based GNSS technique, the InSAR methods enable spatial monitoring of ongoing ground deformations. The remote sensing areal investigations provide a better overview of the local terrain changes, however, the accuracy of radar images is lower than the ground-based GNSS measurements. Therefore, the long-term GNSS observations are a valuable data source in the integration procedure with InSAR methods. The real-time/near real-time GNSS techniques provide the positions with a few seconds/minutes delay using broadcast/ultrarapid products, whereas the Sentinel-1's precise orbits are available after around two weeks from the acquisition time. The latency in InSAR products implies that the GNSS results could be applied to improve InSAR spatial mapping, however, InSAR interferograms could not be used to reduce the RMS errors in RT/NRT monitoring.

In this study, the possibility of ground deformation detection by RT and NRT techniques was examined. During the analysis, several factors were taken into account to characterize the feasibility and accuracy of displacement determination. To perform the quality of RT and NRT estimation, observations were processed in the independent multi-GNSS P-P service using the final CODE products. Furthermore, the accuracy level of the in-house P-P system was investigated. To verify the quality, external data from the EUREF combined solution were used. The RMS errors for the horizontal components did not exceed 2 mm, whereas, in the vertical direction, the errors were in the range of 3–5 mm. Nevertheless, the existence of significant noise (expressed in standard deviation units) between 3 and 5 mm in the EUREF time series should be noted. Thus, the P-P scenario was considered as the reference data source for the PPP-RT, PPP-RT-D, NRT, NRT-D, and NRT-S services.

This article examined two years of ground movement monitoring for the EPOS-PL network. The verification procedure for the RT and NRT systems included investigating the achieved accuracy, the time span required to detect a significant displacement, and the determination of the minimum detectable value of deformation. Compared to the P-P data source, for the horizontal components, the NRT approach had RMS errors of around 2–4 mm, while the RT errors ranged from 5 to 10 mm. In the vertical direction, the NRT had RMS errors of 5–6 mm, while the RT service had RMS errors in the range of 10–16 mm (see Fig. 7). The results confirmed that the automated computing postprocessing and near real-time infrastructure developed in EPOS-PL CIBDG can detect displacements with subcentimeter accuracy.

To conclude, regarding the accuracy level of the long-term deformation calculations and the latency of the estimation process, the NRT-S service achieved the most efficient results. The normal equation files, stored during the 15-min NRT computations, combined within the NRT-S procedure, ensured statistical parameter values comparable to the P-P reference solution. Nevertheless, NRT-S calculations are completed with a significantly shorter latency than in the P-P service; the NRT stacked results are available two hours after the end of the day, whereas P-P results are estimated with the delay of about 2 weeks, depending on the availability of GNSS final products. All GNSS computation strategies presented in this article are fully scalable and can be applied wherever automated displacement monitoring is required. Moreover, the investigation presented in this article provides knowledge about the capability and precision of particular permanent GNSS techniques regarding long-term ground movement detection.

Acknowledgment

The GNSS stations BES1, CES1, KES1, LES1, RES1, and WROE were established as part of the EPOS-PL scientific infrastructure.

References

[1] H. Doležalová, V. Kajzar, K. Souček, and L. Staš, "Evaluation of mining subsidence using GPS data," *Acta Geodynamica et Geomaterialia*, vol. 6, no. 3, pp. 359–367, 2009.

[2] J. Wang, X. Peng, and C. H. Xu, "Coal mining GPS subsidence monitoring technology and its application," *Mining Sci. Technol. (China)*, vol. 21, no. 4, pp. 463–467, 2011, doi: 10.1016/j.mstc.2011.06.001.

[3] I. Kudłacik, J. Kapłon, G. Lizurek, M. Crespi, and G. Kurpiński, "High-rate GPS positioning for tracing anthropogenic seismic activity: The 29 January 2019 mining tremor in Legnica-Głogów copper district, Poland," *Measurement*, vol. 168, 2021, Art. no. 108396, doi: 10.1016/j.measurement.2020.108396.

[4] Z. Szczerbowski and J. Jura, "Mining induced seismic events and surface deformations monitoring by GPS permanent stations," *Acta Geodynamica et Geomaterialia*, vol. 12, no. 3, pp. 237–248, 2015, doi: 10.13168/AGG.2015.0023.

[5] X. Rodriguez-Lloveras, C. Puig-Polo, N. Lantada, J. A. Gili, and J. Marturia, "Two decades of GPS/GNSS and DInSAR monitoring of Cardona salt mines (NE of Spain) - natural and mining-induced mechanisms and processes," *Proc. Int. Assoc. Hydrological Sci.*, vol. 382, pp. 167–172, 2020, doi: 10.5194/piahs-382-167-2020.

[6] C.-H. Xu, J.-L. Wang, J.-X. Gao, J. Wang, and H. Hu, "Precise point positioning and its application in mining deformation monitoring," *Trans. Nonferrous Met. Soc. China*, vol. 21, pp. s499–s505, 2011, doi: 10.1016/S1003-6326(12)61632-X.
[7] M. Ilieva et al., "Combined study of a significant mine collapse based on seismological and geodetic data-29 January 2019, Rudna Mine, Poland," *Remote Sens.*, vol. 12, no. 10, 2020, Art. no. 1570, doi: 10.3390/rs12101570.
[8] N. Shen et al., "A review of global navigation satellite system (GNSS)-based dynamic monitoring technologies for structural health monitoring," *Remote Sens.*, vol. 11, no. 9, 2019, Art. no. 1001, doi: 10.3390/rs11091001.
[9] J. X. Gao, C. Liu, J. Wang, Z. K. Li, and X. C. Meng, "A new method for mining deformation monitoring with GPS-RTK," *Trans. Nonferrous Met. Soc. China*, vol. 21, pp. s659–s664, 2011, doi: 10.1016/S1003-6326(12)61658-6.
[10] X. Lian, Z. Li, H. Yuan, H. Hu, Y. Cai, and X. Liu, "Determination of the stability of high-steep slopes by global navigation satellite system (GNSS) real-time monitoring in long wall mining," *Appl. Sci.*, vol. 10, no. 6, 2020, Art. no. 1952, doi: 10.3390/app10061952.
[11] G. Mutke et al., "Upper silesian geophysical observation system a unit of the EPOS project," *J. Sustain. Mining*, vol. 18, no. 4, pp. 198–207, 2019, doi: 10.1016/j.jsm.2019.07.005.
[12] T. Hadaś, "GNSS-warp software for real-time precise point positioning," *Artif. Satellites*, vol. 50, no. 2, pp. 59–76, 2015, doi: 10.1515/arsa-2015-0005.
[13] K. Kazmierski, T. Hadaś, and K. Sośnica, "Weighting of multi-GNSS observations in real-time precise point positioning," *Remote Sens.*, vol. 10, no. 1, 2018, Art. no. 84, doi: 10.3390/rs10010084.
[14] D. Tondaś, J. Kapłon, and W. Rohm, "Ultra-fast near real-time estimation of troposphere parameters and coordinates from GPS data," *Measurement*, vol. 162, 2020, Art. no. 107849, doi: 10.1016/j.measurement.2020.107849.
[15] S. Lasocki and B. Orlecka-Sikora, "Integrated approach to geophysical hazards induced by exploration and exploitation of georesources - to facilitate the way of attaining excellence," *EPOS Newslett.*, vol. 1, no. 3, pp. 1–5, 2016.
[16] R. Dach, S. Lutz, P. Walser, and P. Fridez, *Bernese GNSS Software Version 5.2. User Manual*. Bern, Switzerland: Astronomical Inst., Univ. Bern, 2015, doi: 10.7892/boris.72297.
[17] R. F. Leandro, R. B. Langley, and M. C. Santos, "UNB3m_pack: A neutral atmosphere delay package for radiometric space techniques," *GPS Solutions*, vol. 12, no. 1, pp. 65–70, 2008, doi: 10.1007/s10291-007-0077-5.
[18] J. Böhm, J. Kouba, and H. Schuh, "Forecast Vienna mapping functions 1 for real-time analysis of space geodetic observations," *J. Geodesy*, vol. 83, no. 5, pp. 397–401, 2009, doi: 10.1007/s00190-008-0216-y.
[19] J. Böhm, B. Werl, and H. Schuh, "Troposphere mapping functions for GPS and very long baseline interferometry from European centre for medium-range weather forecasts operational analysis data," *J. Geophys. Res., Solid Earth*, vol. 111, no. B2, 2006, doi: 10.1029/2005JB003629.
[20] G. Chen and T. A. Herring, "Effects of atmospheric azimuthal asymmetry on the analysis of space geodetic data," *J. Geophys. Res., Solid Earth*, vol. 102, pp. 20489–20502, 1997, doi: 10.1029/97jb01739.
[21] T. A. Springer and U. Hugentobler, "IGS ultra rapid products for (Near-) real-time applications," *Phys. Chem. Earth, Part A, Solid Earth Geodesy*, vol. 26, no. 6, pp. 623–628, 2001, doi: 10.1016/S1464-1895(01)00111-9.
[22] R. Dach et al., "CODE final product series for the IGS," Astronomical Inst., Univ. Bern, Bern, Switzerland, 2020, doi: 10.7892/boris.75876.4.
[23] B. Luzum and G. Petit, "The IERS conventions (2010): Reference systems and new models," *Proc. Int. Astronomical Union*, vol. 10, no. H16, pp. 227–228, 2012, doi: 10.1017/S1743921314005535.
[24] Z. Altamimi, C. Boucher, and P. Willis, "Terrestrial reference frame requirements within GGOS perspective," *J. Geodyn.*, vol. 40, no. 4, pp. 363–374, 2005, doi: 10.1016/j.jog.2005.06.002.
[25] Z. Altamimi, P. Rebischung, L. Métivier, and X. Collilieux, "ITRF2014: A new release of the international terrestrial reference frame modeling nonlinear station motions," *J. Geophysical Res., Solid Earth*, vol. 121, no. 8, pp. 6109–6131, 2016, doi: 10.1002/2016JB013098.
[26] Z. Altamimi, "EUREF technical note 1: Relationship and transformation between the international and the European terrestrial reference systems," Institut Nat. de l'Inf. Géographique et Forestière, Saint-Mandé, France, 2018.
[27] M. Ilieva et al., "Mining deformation life cycle in the light of InSAR and deformation models," *Remote Sens.*, vol. 11, no. 7, 2019, Art. no. 745, doi: 10.3390/rs11070745.

Damian Tondaś received the B.S. and M.S. degrees in geoinformatics from Wrocław University of Environmental and Life Sciences (UPWr), Wrocław, Poland, in 2015 and 2017, respectively. He is currently working toward the Ph.D. degree with thesis on "Integration of GNSS and InSAR observations for monitoring deformations in mining areas," with UPWr.

His main research interests include GNSS ground deformation monitoring and integration of GNSS and InSAR observations.

Kamil Kazmierski received the Ph.D. degree in satellite geodesy from Wrocław University of Environmental and Life Sciences (UPWr), Wrocław, Poland, in 2018.

His research interests include the development of multi-GNSS real-time precise positioning algorithms and monitoring of the quality of real-time orbit and clock corrections. He has coauthored GNSS-WARP (Wroclaw Algorithms for Real-Time Positioning) software for PPP real-time positioning.

Jan Kapłon received the Ph.D. degree in satellite geodesy from Wrocław University of Environmental and Life Sciences (UPWr), Wrocław, Poland, in 2008.

He authored near real-time GNSS data processing systems for retrieving troposphere water vapor content above Poland and Australia for weather forecasting purpose. He is currently an Associate Professor with UPWr, working on near real-time troposphere monitoring and anthropogenic ground deformation monitoring with GNSS as well as on GNSS-seismology.